

Wideband Fast Kernel-Independent Modeling of Large Multiscale Structures Via Nested Equivalent Source Approximation

Original

Wideband Fast Kernel-Independent Modeling of Large Multiscale Structures Via Nested Equivalent Source Approximation / M., Li; Francavilla, MATTEO ALESSANDRO; R., Chen; Vecchi, Giuseppe. - In: IEEE TRANSACTIONS ON ANTENNAS AND PROPAGATION. - ISSN 0018-926X. - 63:(2015), pp. 2122-2134. [10.1109/TAP.2015.2402297]

Availability:

This version is available at: 11583/2605555 since:

Publisher:

IEEE

Published

DOI:10.1109/TAP.2015.2402297

Terms of use:

openAccess

This article is made available under terms and conditions as specified in the corresponding bibliographic description in the repository

Publisher copyright

IEEE postprint/Author's Accepted Manuscript

©2015 IEEE. Personal use of this material is permitted. Permission from IEEE must be obtained for all other uses, in any current or future media, including reprinting/republishing this material for advertising or promotional purposes, creating new collecting works, for resale or lists, or reuse of any copyrighted component of this work in other works.

(Article begins on next page)

Wideband Fast Kernel-Independent Modeling of Large Multiscale Structures via Nested Equivalent Source Approximation

Mengmeng Li, Matteo Alessandro Francavilla, *Member, IEEE*, Rushan Chen, *Member, IEEE*, and Giuseppe Vecchi, *Fellow, IEEE*

Abstract—We propose a wideband fast kernel-independent modeling of large multiscale structures; we employ a nested equivalent source approximation (NESA) to compress the dense system matrix. The NESA was introduced by these authors for low and moderate frequency problems (smaller than a few wavelengths); here we introduce a high-frequency NESA algorithm, and propose a hybrid version with extreme wideband properties. The equivalent sources of the wideband NESA (WNESA) are obtained by an inverse-source process, enforcing equivalence of radiated fields on suitably defined testing surfaces. In the low frequency region, the NESA is used unmodified, with a complexity of $\mathcal{O}(N)$. In the high frequency region, in order to obtain a fixed rank matrix compression, we hierarchically divide the far coupling space into pyramids with angles related to the peer coupling group size, and the NESA testing surfaces are defined as the boundaries of the pyramids. This results in a directional nested low rank (fixed rank) approximation with $\mathcal{O}(N \log N)$ computational complexity that is kernel independent; overall, the approach yields wideband fast solver for the modeling of large structures that inherits the efficiency and accuracy of low-frequency NESA for multiscale problems. Numerical results and discussions demonstrate the validity of the proposed work.

Index Terms—Integral equations, fast solvers, wideband methods, low-rank approximation, multiscale.

I. INTRODUCTION

IN recent years there has been a strong interest in wideband electromagnetic algorithms for the full-wave simulation of realistic multiscale structures. The peculiar feature of large multiscale problems is the coexistence of dense meshes to capture the geometric details (as in low frequency problems) and of large scale interactions (typical of high frequency problems). The difficulties associated to this scale variability are enhanced in analyses requiring a large frequency range, often with the requirement to change as little as possible the mesh over the frequency range of interest.

Manuscript received on xxxx. This work was supported by Natural Science Foundation of 61431006, 61271076, and 61371037, Jiangsu Natural Science Foundation of BK2012034, Ph.D. Programs Foundation of Ministry of Education of China of 20123219110018, the Fundamental Research Funds for the central Universities of No. 30920140111003 and 30920140121004. The European Communitys Seventh Framework Programme FP7/2007-2013, under Grant 205294, HIRF SE project, and the ICT COST Action IC1102 VISTA.

M. Li and R. Chen are with the Department of Communication Engineering, Nanjing University of Science and Technology, Nanjing, China (email: limengmeng@njust.edu.cn; eerschen@njust.edu.cn).

M. A. Francavilla is with the Antenna and EMC Lab (LACE), Istituto Superiore Mario Boella (ISMB), Torino, Italy (email: francavilla@ismb.it).

G. Vecchi is with the Antenna and EMC Lab (LACE), Politecnico di Torino, Torino, Italy (email: giuseppe.vecchi@polito.it).

Many fast factorization schemes have been proposed in literature to reduce the cost of MVP in iterative solutions. Fast solvers can be grouped into two large classes: kernel-based compression schemes (based on some suitable expansion of the underlying integral kernel), and algebraic compression schemes, which only require knowledge of a subset of matrix entries. The latter, sometimes also known as rank based methods [1]–[7], are typically quite efficient for low frequency problems, while they progressively lose efficiency with the increasing electrical size of the simulation domain. Conversely, kernel-based factorizations such as FFT based methods [8]–[10] or the multilevel fast multipole algorithm (MLFMA) [11], [12], are more efficient, reducing memory requirements and MVP time to $\mathcal{O}(N^{1.5} \log N)$ and $\mathcal{O}(N \log N)$, respectively. Another fast method is the MultiLevel Matrix Decomposition Algorithm (MLMDA) [13], that has been widely adopted because of its excellent efficiency-vs-complicacy ratio (e.g. [14]).

However, the above mentioned fast IE solvers require special attention for wideband simulations: as well known, MLFMA is not stable at low frequency (e.g. when group size of the geometrical clustering is below $\sim 0.3\lambda$), requiring substantial modifications to the algorithm in the low frequency regime [15]–[17]. A different solution, vastly adopted in literature, consists in combining standard low frequency solvers (e.g., Accelerated Cartesian Expansion (ACE) [18]–[20], FFT interpolation [21], and MultiLevel Matrix Compression Method (MLMCM) [22]) with MLFMA to account for large scale couplings.

On the other hand, interest in algebraic decompositions has grown recently: interpolation methods [4], [23], equivalent source densities [24], randomized QR decompositions [25], [26], only to cite a few. Their main appeal lies in the simplicity to adapt to different kernels (EFIE and MFIE [26], penetrable bodies, wire-patch junctions [27], and layered media problems).

In this work, we limit our focus to rank based methods. Traditional rank based methods [1]–[7] suffer from performance degradation when frequency increases: 1) the rank of the far coupling sub-matrices increases very fast, due to the oscillatory nature of the kernel, leading to a complexity which can scale as poorly as $\mathcal{O}(N^2)$ and $\mathcal{O}(N^3)$ for memory and CPU time, respectively [5]; 2) even when using a multilevel algorithm, the low rank approximations need be explicitly computed and stored at each level, which in turn worsens setup

time and storage requirements [1]–[7].

Recently, we proposed a Nested Equivalent Source Approximation (NESA [28]), in which the low rank approximation at each level is expressed recursively in terms of its child levels, and eventually in terms of the low rank approximation at leaf level. The resulting algorithm has proven $\mathcal{O}(N)$ complexity for static to moderate frequency problems; in this work we present an extension which allows to handle large scale couplings. When combined with the algorithm [28] for low frequency couplings, it results in a wideband fast solver with complexity bounded by $\mathcal{O}(N \log N)$. Our method shares the same motivations of other well-known wideband solvers [15]–[22]; however, our efforts aim at providing a kernel-independent wideband algorithm. The nested approximation was inspired by [29], [30]; differently from the mentioned works, which employ ACA [3], [5] to obtain the low rank approximation, we introduce equivalent sources on automatically defined surfaces, thanks to an inverse-source process [24], [31] that enforces equivalence of radiated fields on (properly defined) testing surfaces, within a prescribed accuracy. A similar idea applied to Volume Integral Equations (VIE) was exploited in [32] to reduce the number of unknowns, by mapping volume unknowns onto surfaces recursively.

The key point exploited here to compress high frequency couplings consists in partitioning the interactions in *directions*: the Green’s function is indeed smooth, and thus compressible, when observation is limited to a specific (narrow enough) direction [25]. In each direction, the rank is independent of the group size.

Differently from fast directional multilevel algorithms [25], [26], [33], which use randomized QR decomposition to approximate the Green’s function in each direction, we use NESA [28] to directly compress matrix entries, yielding a kernel independent fast solver. Finally, our new proposed method is employed to simulate large real-life high-fidelity multiscale structures, to address the important issue of stability and efficiency.

The remainder of the paper is organized as follows: in Section II, we describe the proposed algorithm; numerical results and discussions in Section III demonstrate the validity of the proposed method. Finally, a brief conclusion is given in Section IV.

II. WIDEBAND NESTED EQUIVALENT SOURCE APPROXIMATION

In this section we first define some parameters as in Table I. Starting from an Octree clustering of the basis functions (e.g., RWG [34]), if groups s and t satisfy the far coupling admissibility condition (which will be discussed in the following) the low rank approximation of the resulting sub-matrix of MoM [34] $\mathbf{Z}_{s,t}$ can be expressed as:

$$\mathbf{Z}_{s,t} = \mathbf{U}_s \mathbf{D}_{s,t} \mathbf{V}_t \quad (1)$$

where matrix \mathbf{U}_s only relates to group s and is labeled “receiving matrix”, \mathbf{V}_t only relates to group t and is labeled “radiation matrix”, and $\mathbf{D}_{s,t}$ is the “translation matrix” [28]. The aim of this work is to express radiation and receiving matrices in

TABLE I
PARAMETER NOTATION IN WNES A

| | |
|---------------------------|---|
| \sum_{σ}^i | The <i>equivalent</i> sphere of radius R_r for group i |
| $\sum_{\sigma^d}^i$ | The <i>testing</i> pyramid surface for group i in direction d |
| $\boldsymbol{\tau}_i$ | RWG basis functions on equivalent sphere surface of group i |
| $\boldsymbol{\sigma}_i^d$ | RWG test functions on testing pyramid surface of group i in direction d |
| $\mathbf{Z}_{i,j}$ | sub-matrix between groups i and j |
| \mathbf{I}_i | Current density coefficients for basis function in group i |
| \mathbf{E}_i | Projection of the electric field onto test functions in group i |
| d | Directions number is d |
| $-d$ | Opposite direction of direction d |
| L | Total number of levels in the Octree |
| N_d^l | Number of non-zero directions at level l |
| D_l | group size (edge of a cube) at level l |

terms of radiation and receiving matrices of its child groups, and recursively in terms of radiation and receiving matrices at leaf level, extending the nested approximation of [28] to high frequency couplings. As mentioned in section I and detailed in the following, sub-blocks of the system matrix representing interactions between two clustered groups of “well separated” basis functions are rank deficient. Nevertheless, the rank of these blocks increases very fast with group size if one directly uses the admissibility condition employed in traditional low rank compression schemes [1]–[7], which in turn leads to unacceptable computational costs for large 3D problems [1]–[7]. In order to bound high frequency ranks, the key point consists in “limiting” the direction of observation within *narrow* angles, the number of directions depending on the observation scale (i.e., on the Octree level); following the ideas presented in [30], we express the nested approximation from groups t and s in directions d and $-d$ to their parent groups t^p and s^p in directions d^p and $-d^p$ as:

$$\mathbf{U}_{s^p}^{l,-d^p} = \mathbf{U}_s^{l+1,-d} \mathbf{B}^{(l+1,l),-d^p} \quad (2)$$

$$\mathbf{V}_{t^p}^{l,d^p} = \mathbf{C}^{(l,l+1),d^p} \mathbf{V}_t^{l+1,d} \quad (3)$$

Matrices $\mathbf{B}^{(l,l-1),-d^p}$ and $\mathbf{C}^{(l-1,l),d^p}$ are called “transfer matrices” (see Table I for the meaning of parameters); eq. (2)-(3) allow to express the radiation/receiving matrix at level l in terms of the radiation/receiving matrices of its child level ($l+1$). If we denote with D_l the group size (the edge of an Octree cube) at level l , the low rank approximation of eq. (2)-(3) can be specialized to three different cases, depending on group size:

- 1) **High frequency couplings:** level l and its child $l+1$ belong to the high frequency regime ($D_l, D_{l+1} \geq D_0$;
- 2) **Interface couplings:** level l and its child $l+1$ belong to the high frequency and low frequency regimes, respectively $D_l \geq D_0, D_{l+1} < D_0$;
- 3) **Low frequency couplings:** level l and its child $l+1$ belong to the low frequency regime ($D_l, D_{l+1} < D_0$).

D_0 is the threshold group size to discriminate high frequency from low frequency couplings; in the following, D_0 will be set to $D_0 = \lambda$, unless otherwise specified.

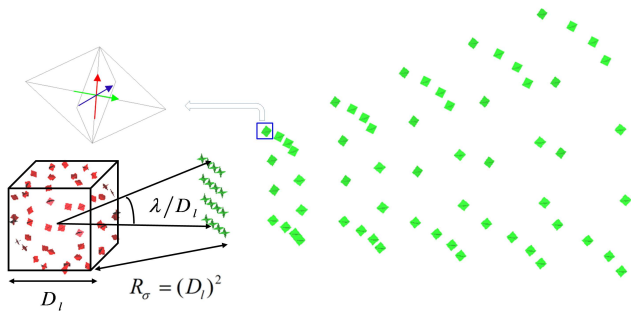


Fig. 1. Distribution of the equivalent and testing basis functions of a group for high frequency coupling in 3D view on the equivalence surface (inner sphere), the testing surface is a pyramids with angle $O(\lambda/D_l)$, and the distance from the equivalent sphere to the pyramids is $R_\sigma = (D_l)^2$ for high frequency region. In the corner details the three independent RWG basis functions at a point, arrows represent normal to defining edges.

A. Admissibility Conditions and Equivalent Source Distributions

In this subsection, we will first describe the admissibility conditions, and then introduce the “equivalent source” distributions. For the admissibility conditions, we follow the works in [23], [25], [26], [30], although our nested approximation is constructed in a different way. When considering the coupling between groups s and t , if $D_l < D_0$ we define it as a *low frequency* coupling, and the admissibility condition for compressibility is the same as in traditional rank based algorithms [1]–[7]: group t is in the far interaction list of group s if groups t and s are not neighbours, i.e. if their defining cubes do not share any vertex.

$$R(s, t) \geq 2D_l \quad (4)$$

where $R(s, t)$ is the center-to-center distance between groups s and t . Low frequency couplings are computed using the algorithm [28].

Conversely, when $D_l \geq D_0$, the existence of a separated representation of the kernel is guaranteed by the *directional low rank property* [25], [33]: given a source group s with radius r , interactions through Helmholtz kernel with groups t_i which are at a distance $\frac{R(s, t_i)}{\lambda} > \left(\frac{r}{\lambda}\right)^2$, and within a cone spanning an angle λ/r and centered in the center of group s , admit a separable low rank representation (within a prescribed accuracy), with rank independent of r . High frequency couplings are then computed via a directional algorithm; the admissibility condition for compression of interactions between groups s and t is defined by:

$$\frac{R(s, t)}{\lambda} \geq \left(\frac{D_l}{\lambda}\right)^2 \quad (5)$$

Then, the directional low rank property is invoked to define cones spanning an angle $\mathcal{O}\left(\frac{\lambda}{D_l}\right)$. The peer far coupling region of group s and t at level l of high frequency regime is defined

as

$$\frac{R(s, t)}{\lambda} \geq \left(\frac{D_l}{\lambda}\right)^2 \quad (6a)$$

$$\frac{R(s_p, t_p)}{\lambda} < \left(\frac{D_{l-1}}{\lambda}\right)^2 \quad (6b)$$

where $D_{l-1} = 2D_l$ is the parent group size at level $l-1$, i.e. the far coupling interaction list of a source group s includes groups t satisfying the admissibility condition (5), subject to their parents s^p and t^p not satisfying (5). For simplicity of implementation, due to geometrical considerations arising from an Octree clustering of the unknowns (clustered in cubes rather than spheres), it is convenient to define directions as the volumes enclosed by square pyramids, with bases described by the faces of Octree cubes. One important advantage in employing square pyramids is the fact that they allow to define “hierarchical directions”, i.e. each direction of a group is completely enclosed by the directions of its child groups [25]. This in turn guarantees that, if two groups satisfy the admissibility condition of eq. (5), then also their children satisfy the admissibility condition: this is a key point to define a nested directional approximation, as detailed in the following Sec. II-B and Sec. II-C.

In this work, rather than selecting “dominant basis functions” via ACA as in [29], [30], we design proper equivalent and testing surface to obtain the equivalent basis functions. Although the complexity scaling would be unaffected if ACA was employed to select dominant sources, the algorithm would lead to a time consuming low rank approximation. Besides, ACA does not allow exploiting symmetries when building the approximation, resulting in a higher memory demanding approximation. It is well known that, in the low frequency regime, the number of equivalent sources Q (i.e., the rank) is independent of the group size [1]–[7], [28]. In the high frequency regime, the rank Q can be made independent of the group size too, exploiting the directional low rank property. Even more important, the introduced equivalent and testing surfaces lead to an intrinsically multiscale family of auxiliary sources, improving field representation in multiscale problems, which in turn leads to a significant improvement in convergence speed [28].

B. High Frequency Wideband Nested Equivalent Source Approximation via Inverse-source Process in Directions

Fig. 2 shows a schematic representation of the process to evaluate couplings between groups t and s at peer level, when in the high frequency regime. The equivalent source distributions, located on surfaces $\Sigma_\tau^{t,s}$, are shown in red; the testing functions where field equivalence is enforced, indicated with $\Sigma_{\sigma \pm d}^{t,s}$, are shown in green. For the sake of simplicity, actual sources are not shown in Fig. 2. By convention, if group s is in direction d of group t , we will indicate the opposite direction as $-d$, i.e. group t is in direction $-d$ of group s . Equivalent sources τ_t are obtained by enforcing (in a weak sense) equivalence of fields radiated by τ_t and actual sources, on the faces of the wedge enclosing direction d . This procedure (indicated with 1 in Fig. 2) clearly involves a forward radiation

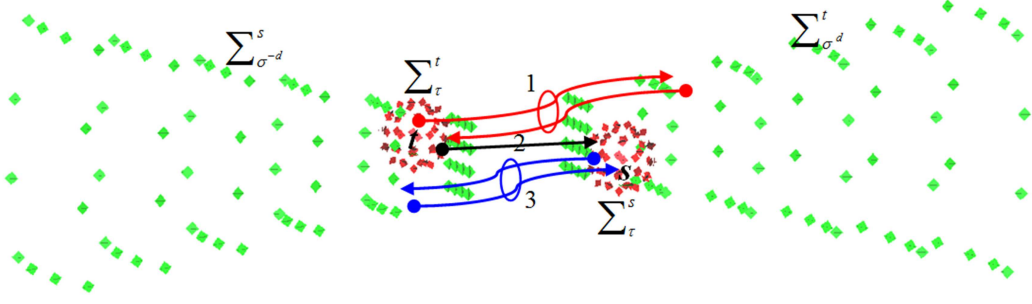


Fig. 2. Coupling between two groups t and s at peer level using equivalent RWG basis functions and inverse-source equivalence in high frequency region. Equivalent source distributions are sought on inner sphere Σ_τ^t and Σ_σ^s , by enforcing testing radiation field on the boundary of the pyramids $\Sigma_{\sigma^d}^t$ in direction d and $\Sigma_{\sigma^{-d}}^s$ in direction $-d$, respectively. The inverse-source determination process for group t is symbolized by 1 (contains forward and backward radiation processes), this leads to assembly of the radiation matrix \mathbf{V}^d in direction d for groups s ; likewise, 3 symbolize the process to compute the receiving matrix \mathbf{U}^{-d} in direction $-d$ of group t . The inter-group translation matrix construction is symbolized by 2.

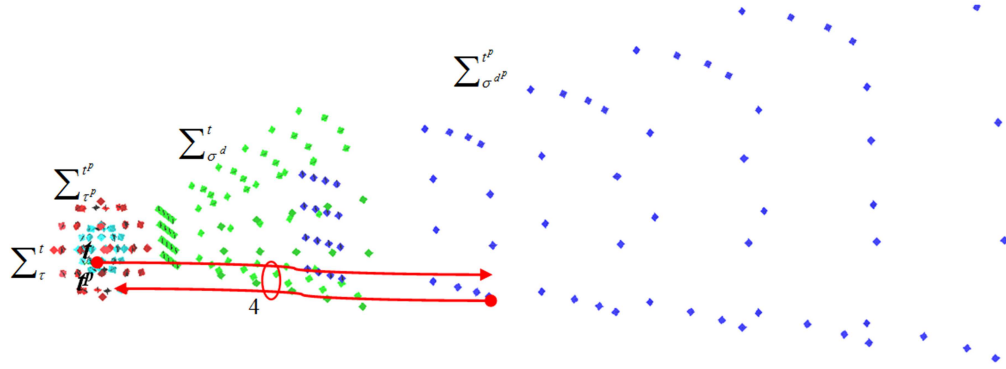


Fig. 3. Illustration of the radiation process of parent group t^p with the radiation matrices of its child group t . The inverse-source determination process, by testing the field radiated by equivalent source surface Σ_τ^t and $\Sigma_{\tau^p}^{t^p}$ on testing surface $\Sigma_{\sigma^{d^p}}^{t^p}$ in direction d^p , the process is symbolized by 4. d^p is the direction of parent group t^p , it is contained in direction d of the child group t .

operator (to evaluate fields radiated by actual sources), and an inverse problem, to reconstruct equivalent sources τ_t from fields on $\Sigma_{\sigma^d}^s$. Formally, we can write the equivalence of fields as:

$$\mathbf{Z}_{\sigma_t^d, t} \mathbf{I}_t = \mathbf{Z}_{\sigma_t^d, \tau_t} \mathbf{I}_{\tau_t}^d \quad (7)$$

Then, we can solve for $\mathbf{I}_{\tau_t}^d$, collecting the coefficients of equivalent sources τ_t , which radiate the same field as actual sources in the region delimited by the wedge enclosing direction d :

$$\mathbf{I}_{\tau_t}^d = \mathbf{Z}_{\sigma_t^d, \tau_t}^\dagger \mathbf{Z}_{\sigma_t^d, t} \mathbf{I}_t \quad (8)$$

where $(\cdot)^\dagger$ denotes pseudo-inverse; in this work we compute pseudo-inverses by means of a truncated SVD. By reciprocity, if fields $\mathbf{E}_{\tau_s}^{-d}$ tested on Σ_τ^s are known (where the dependence on direction $-d$ has been made explicit), we can find coefficients $\mathbf{I}_{\sigma_s^{-d}}$ of equivalent sources σ_s^{-d} on $\Sigma_{\sigma^{-d}}^s$ radiating the same field $\mathbf{E}_{\tau_s}^{-d}$:

$$\mathbf{E}_{\tau_s}^{-d} = \mathbf{Z}_{\tau_s, \sigma_s^{-d}} \mathbf{I}_{\sigma_s^{-d}} \quad (9)$$

By solving eq. (9) for $\mathbf{I}_{\sigma_s^{-d}}$, the field tested on actual testing functions of group s reads as:

$$\mathbf{E}_s^{-d} = \mathbf{Z}_{s, \sigma_s^{-d}} \mathbf{Z}_{\tau_s, \sigma_s^{-d}}^\dagger \mathbf{E}_{\tau_s}^{-d}. \quad (10)$$

Finally, after defining a *translation matrix* $\mathbf{D}_{s,t}$ collecting couplings between equivalent sources τ_t and τ_s as:

$$\mathbf{D}_{s,t} = \mathbf{Z}_{\tau_s, \tau_t} \quad (11)$$

we can express fields in group s due to sources in group t from eq. (9), (10), and (11)

$$\begin{aligned} \mathbf{E}_s^{-d} &= \mathbf{Z}_{s,t} \mathbf{I}_t = \mathbf{Z}_{s, \sigma_s^{-d}} \mathbf{Z}_{\tau_s, \sigma_s^{-d}}^\dagger \mathbf{D}_{s,t} \mathbf{I}_{\tau_t}^d \\ &= \mathbf{Z}_{s, \sigma_s^{-d}} \mathbf{Z}_{\tau_s, \sigma_s^{-d}}^\dagger \mathbf{D}_{s,t} \mathbf{Z}_{\sigma_t^d, \tau_t}^\dagger \mathbf{Z}_{\sigma_t^d, t} \mathbf{I}_t \end{aligned} \quad (12)$$

Eq. (12) is the single level WNSA approximation of $\mathbf{Z}_{s,t}$:

$$\begin{aligned} \mathbf{Z}_{s,t} &= \mathbf{Z}_{s, \sigma_s^{-d}} \mathbf{Z}_{\tau_s, \sigma_s^{-d}}^\dagger \mathbf{D}_{s,t} \mathbf{Z}_{\sigma_t^d, \tau_t}^\dagger \mathbf{Z}_{\sigma_t^d, t} \\ &= \mathbf{U}_s^{-d} \mathbf{D}_{s,t} \mathbf{V}_t^d \end{aligned} \quad (13)$$

where $\mathbf{U}_s^{-d} = \mathbf{Z}_{s, \sigma_s^{-d}} \mathbf{Z}_{\tau_s, \sigma_s^{-d}}^\dagger$ is the *receiving matrix* of group s in direction $-d$, and $\mathbf{V}_t^d = \mathbf{Z}_{\sigma_t^d, \tau_t}^\dagger \mathbf{Z}_{\sigma_t^d, t}$ is the *radiation matrix* of group t in direction d .

C. Multilevel WNSA

Differently from traditional rank based methods [1]–[7], in WNSA we express radiation and receiving matrices at the generic level $l \neq L$ recursively in terms of radiation and receiving matrices at leaf level; this is done by introducing proper *transfer matrices* which allow to ascend/descend the

tree, as mentioned in Sec. II. Fig. 3 illustrates the main idea of a two level nested approximation for radiation matrix in high frequency regime: the testing surface $\Sigma_{\sigma^{d^p}}^{t^p}$ in direction d^p of group t^p (parent group of t) is enclosed by the testing surface $\Sigma_{\sigma^d}^t$ in direction d of group t . Accordingly, the radiation matrix in direction d of group t can be used to approximate couplings of group t^p in direction d^p , since the conditions of the directional low rank property are satisfied. With the help of Fig. 3, in analogy with eq. (7) and (8) we can obtain the coefficients $\mathbf{I}_{\tau_t^p}^{d^p}$ of equivalent sources τ_{t^p} at parent level by enforcing equivalence of fields radiated by τ_{t^p} and τ_t on the surface $\Sigma_{\sigma^{d^p}}^{t^p}$, indicated with 4 in Fig. 3. Formally:

$$\mathbf{I}_{\tau_t^p}^{d^p} = \mathbf{Z}_{\sigma_{t^p}^{d^p}, \tau_{t^p}}^\dagger \mathbf{Z}_{\sigma_{t^p}^{d^p}, \tau_t} \mathbf{I}_{\tau_t^d} \quad (14)$$

Analogous derivations allow expressing fields $\mathbf{E}_{\tau_s^d}^{-d}$ on Σ_{τ^s} in terms of $\mathbf{E}_{\tau_{s^p}}^{-d^p}$ on $\Sigma_{\tau^{s^p}}$:

$$\mathbf{E}_{\tau_s^d}^{-d} = \mathbf{Z}_{\tau_s, \sigma_{s^p}^{-d^p}} \mathbf{Z}_{\tau_{s^p}, \sigma_{s^p}^{-d^p}}^\dagger \mathbf{E}_{\tau_{s^p}}^{-d^p}. \quad (15)$$

Finally, after defining the translation matrix at parent level from τ_{s^p} to τ_{t^p} as

$$\mathbf{D}_{s^p, t^p} = \mathbf{Z}_{\tau_{s^p}, \tau_{t^p}} \quad (16)$$

the two-level high frequency WNESAs approximation is straight forward:

$$\mathbf{Z}_{s^p, t^p} = \mathbf{U}_s^{-d} \mathbf{B}_{s, s^p}^{-d^p} \mathbf{D}_{s^p, t^p} \mathbf{C}_{t^p, t}^{d^p} \mathbf{V}_t^d \quad (17)$$

where we have introduced the transfer matrices $\mathbf{C}_{t^p, t}^{d^p} = \mathbf{Z}_{\sigma_{t^p}^{d^p}, \tau_{t^p}}^\dagger \mathbf{Z}_{\sigma_{t^p}^{d^p}, \tau_t}$ from child direction d to parent direction d^p , and $\mathbf{B}_{s, s^p}^{-d^p} = \mathbf{Z}_{\tau_s, \sigma_{s^p}^{-d^p}} \mathbf{Z}_{\tau_{s^p}, \sigma_{s^p}^{-d^p}}^\dagger$ from parent direction $-d^p$ to child direction $-d$. Eq. (17) can be easily extended to a generic number of levels l as:

$$\begin{aligned} \mathbf{Z}_{s, t}^l &= \mathbf{U}_s^{L, -d^L} \mathbf{B}_s^{(L, L-1), (-d^L, -d^{L-1})} \dots \\ &\quad \mathbf{B}_s^{(l+1, l), (-d^l, -d^{l+1})} \mathbf{D}_{s, t}^l \mathbf{C}_t^{(l, l+1), (d^l, d^{l+1})} \dots \\ &\quad \mathbf{C}_t^{(L-1, L), (d^{L-1}, d^L)} \mathbf{V}_t^{L, d^L} \end{aligned} \quad (18)$$

As mentioned at the beginning of this section, when computing couplings at the bottom of the tree the directional low rank approximation is not invoked, and couplings are evaluated as in [28]. If we denote as l_{in} the level at the interface between low and high frequency regions, we can generalize eq. (18) to a *mixed frequency* scenario as in eq. (19).

Note that, when WNESAs is applied to an EFIE problem, radiation and receiving matrices in a specified direction are linked by a transpose operation; we then need to compute and store only one of the two. The above WNESAs algorithm is schematically summarized in Algorithm 1 in Appendix.

D. Further Acceleration in Evaluating WNESAs Approximation

As discussed in [28], symmetry considerations suggest to introduce some strategies to further accelerate the algorithm and increase memory savings. At each level l :

- 1) The relative locations of RWGs on the equivalent and testing spheres are the same within a certain level: only N_d^l pseudo-inverses appearing in eq. (8) and (14) need

be computed, where N_d^l is the number of non-empty directions at level l .

- 2) For each direction d , each group has at most 8 children: no more than $8N_d^l$ transfer matrices need be computed and stored for 3D problems.
- 3) The number of *potential* translators is $N_D^l = (8D_l + 1)^3 - (2D_l + 1)^3$; however, considering that the number of groups per level grows as D_l^{-2} (unknowns are distributed on surfaces only), and that the cardinality of far field interaction lists scales as D_l^2 (as detailed later, see Sec. II-E, eq. (23)), if one computes and stores only the necessary translators, the number of stored translators per level is actually constant. Besides, it can be verified that translation matrices are not full rank: they are further compressed through ACA [28].
- 4) At the top levels of the tree, corresponding to the high frequency regime, the number of translation matrices N_D^l can be very large; a single level nested cross approximation [29], [30] is used to compress the translation matrix:

$$\mathbf{D}_{s, t} = \mathbf{U}_s^{-d} \tilde{\mathbf{D}}_{s, t} \mathbf{V}_t^d \quad (20)$$

For each direction d , only one pair of matrices \mathbf{U}_s^d and \mathbf{V}_t^d need be computed and stored; although N_D^l matrices $\tilde{\mathbf{D}}_{s, t}$ need be computed and stored, their size is smaller than the size of $\mathbf{D}_{s, t}$, yielding huge memory savings and MVP time reduction. A similar acceleration technique, based on QR decomposition, is employed in [23].

From (1) to (4), it is evident that WNESAs approximation time and storage requirements, as well as MVP time, are related to the maximum number of non-empty directions at each level; therefore, it is expected that the algorithm is more efficient for elongated structures such as cylinders, ogives, or missile-like geometries [25]. Conversely, it can be verified that a spherical geometry represents the worst case scenario, as the number of non-empty directions is maximum. However, the number of non-empty directions does not affect the asymptotic complexity of the algorithm, as analyzed in Sec. II-E and Sec. III-B.

Finally, we briefly address the issue of scalability in parallel environments. Parallelization of the matrix compression (setup phase) is quite straightforward, both in shared memory environments (e.g., OpenMP [35]) and distributed memory environments (e.g., MPI [36]): levels are processed sequentially, and each task is assigned a different group (low frequency regime) or direction (high frequency regime). Parallelization of the MVP is less trivial though, especially in distributed memory environments, and presents challenges very similar to MLFMA.

E. Matrix-Vector Product and Complexity Analysis

In order to discuss the complexity analysis of the algorithm, we first report in Algorithm 2 in Appendix a pseudocode of the algorithm to compute MVP $\mathbf{y} = \mathbf{Z}\mathbf{I}$. The parameters in Algorithm 2 and following are defined in Table II. The complexity of the low frequency regime is proven to be $O(N)$ [28], [29]; without loss of generality, in the following we only focus on the high frequency regime interactions.

$$\mathbf{Z}_{s,t}^l = \overbrace{\mathbf{U}_s^L \mathbf{B}_s^{(L,L-1)} \dots \mathbf{B}_s^{(l_{in}+1,l_{in}),d^{-l_{in}}}}^{\text{low frequency}} \overbrace{\dots}^{\text{interface}} \overbrace{\dots \mathbf{B}_s^{(l+1,l),(-d^{l+1},-d^l)} \mathbf{D}_{s,t}^l \mathbf{C}_t^{(l,l+1),(d^l,d^{l+1})} \dots}^{\text{high frequency}} \underbrace{\mathbf{C}_t^{(l_{in},l_{in}+1),d^{l_{in}}}}_{\text{interface}} \underbrace{\dots \mathbf{C}_t^{(L-1,L)} \mathbf{V}_t^L}_{\text{low frequency}} \quad (19)$$

TABLE II
PARAMETER NOTATION IN THE MVP AND FOLLOWING

| | |
|------------------------|---|
| s^l | Non-empty source group s at level l |
| t^l | Non-empty observation group t at level l |
| \mathbf{I}_i | Subvector of \mathbf{I} restricted to basis functions in group i |
| \mathbf{V}_i^{l,d^l} | Radiation matrix for group i at level l in direction d^l |
| \mathbf{B}_i^{l,d^l} | Transfer matrix for group i at level l in direction d^l |
| ζ_i^{l,d^l} | Temporary vector in MVP in the radiation process of group i at level l in direction d^l |
| $\mathbf{D}_i^{l,j}$ | Translation matrix between groups i and j at level l |
| ξ_i^{l,d^l} | Temporary vector in MVP in the translation process of group i at level l in direction d^l |
| \mathbf{U}_i^{l,d^l} | Receiving matrix for group i at level l in direction d^l |
| \mathbf{C}_i^{l,d^l} | Transfer matrix for group i at level l in direction d^l |
| \mathbf{y}_i^{l,d^l} | Temporary vector in MVP in the receiving process receiving of group i at level l in direction d^l |
| \mathbf{y} | Result of the MVP $\mathbf{y} = \mathbf{Z}\mathbf{I}$ |
| $ch(i)$ | Direction number where direction i contained in its child group direction |
| N_i | Number of basis functions in group i |
| M_i | Number of non-empty groups at level l |
| Q | Number of equivalent sources |

For a generic 3D case, if a surface integral equation problem is formulated, it is well known that the number of unknowns scales as $N = \mathcal{O}(S_{max}^2)$, where S_{max} is the maximum electrical size of the object, i.e. the size of the object normalized with respect to wavelength. Before studying the complexity of the algorithm, we recall the scaling of three important quantities:

- at level l , the number of nonempty groups scales as $\mathcal{O}((S_{max}/D_l)^2)$;
- at level l , the maximum number of directions is $\mathcal{O}(D_l^2)$ (see Sec. II-A);
- at level l , in each direction d the number of equivalent sources Q is constant (see Sec. II-A).

With the above in mind, and assuming that the average number of unknowns K per group at leaf level is constant (i.e., it does not depend on the S_{max}) it is easy to verify that the cost of the radiation process (lines 3 to 20 in Algorithm 2) at level l can be bounded by:

$$\mathcal{O}\left((S_{max}/D_L)^2 D_L^2 K Q\right) = \mathcal{O}(N) \quad l = L \quad (21a)$$

$$\mathcal{O}\left((S_{max}/D_l)^2 D_l^2 Q^2\right) = \mathcal{O}(N) \quad l = 1 \dots (L-1) \quad (21b)$$

Noting that the number of levels grows as $L = \mathcal{O}(\log S_{max})$, the overall cost of the radiation process in MVP is $\mathcal{O}(S_{max}^2 \log S_{max}) = \mathcal{O}(N \log N)$. By reciprocity, it is easy

to verify that the cost of receiving process (lines 29 to 48) is the same as the cost of radiation process.

For what concerns storage requirements, it is clear that radiation patterns \mathbf{V}_t have a linear cost both for fill-in time and memory (see eq. (21a)). On the other hand, exploiting symmetry as detailed in [28], only $8N_d^l$ transfer matrices need be computed and stored at level l , and memory for transfer matrices can be bounded as:

$$\mathcal{O}(8D_l^2 Q^2) = \mathcal{O}\left(\left(\frac{S_{max}}{2^{l+1}}\right)^2 Q^2\right) \quad (22)$$

It is then easy to compute the partial sum $\sum_{l=1}^L \left(\frac{S_{max}}{2^{l+1}}\right)^2 = \mathcal{O}(N)$, to prove that memory for transfer matrices has linear complexity.

Finally, we focus on the translation process: as discussed in Sec. II-A, the far interaction list at level l includes groups at a distance smaller than $(2D_l)^2$, where $2D_l$ is parent group size at level $(l-1)$. Then, starting from the admissibility condition of eq. (5), a few manipulations allow to derive an upper bound for the cardinality of the far interaction list at level l for surface problems as

$$N_{FIL}^l = 60 \left(\frac{D_l}{\lambda}\right)^2 + 28 \left(\frac{D_l}{\lambda}\right) + 3 = \mathcal{O}(D_l^2) \quad (23)$$

Then, for a number of non-empty groups growing as $\mathcal{O}((S_{max}/D_l)^2)$, the cost of the translation process at level l is

$$\mathcal{O}\left((S_{max}/D_l)^2 D_l^2 Q^2\right) = \mathcal{O}(N) \quad (24)$$

Summing over $L = \mathcal{O}(\log N)$ levels, the total cost of the translation process is $\mathcal{O}(N \log N)$.

III. NUMERICAL RESULTS AND DISCUSSIONS

In this section different test cases are presented to show the effectiveness of the proposed solver. We first discuss some parameters which are fixed for all simulations: the Octree clustering is always stopped when the average number of basis functions at the finest level is ~ 50 . We indicate average mesh edge length by h , and wavelength by λ . In all numerical experiments, a flexible-GMRES iterative solution is sought, with a maximum number of iterations for the inner solver equal to 10. All simulations have been carried out single threaded on a 64-bits Dell Precision T7400 workstation, Intel Xeon CPU E5440 @ 2.88GHz, 96GB of RAM; double precision computation is always used.

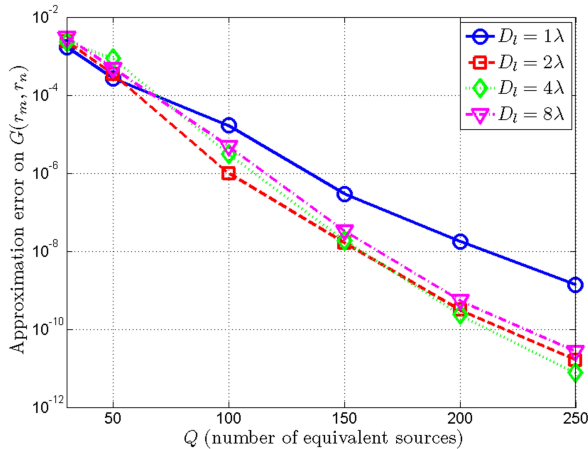


Fig. 4. The approximation error of WNESA for Green’s function matrix $\mathbf{G}(\mathbf{r}_s, \mathbf{r}_t)$, where \mathbf{r}_s and \mathbf{r}_t are 500 random distributed points in groups s and t satisfying the far coupling admission condition, the group size is 1λ , 2λ , 4λ , and 8λ .

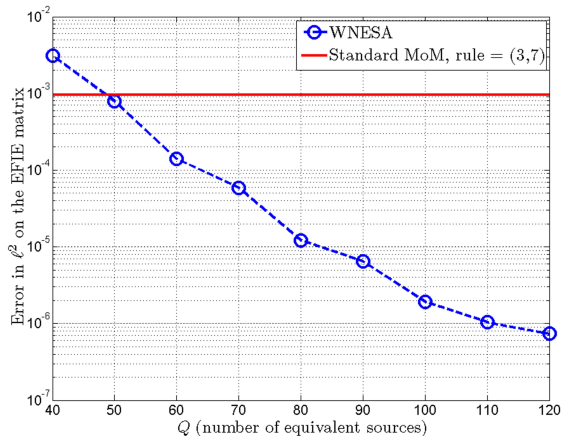


Fig. 5. The approximation error of WNESA for EFIE impedance matrix for two group with group size 1λ , and with 636 and 527 RWG basis functions respectively, are from a cylinder (diameter 1λ , height 8λ) with 13168 unknowns. The reference is a standard MoM with a very accurate quadrature rule, with 61 gaussian points.

A. Accuracy

In order to validate the accuracy of the proposed WNESA, we first test the accuracy of WNESA approximation on the scalar Green’s function; 500 source points \mathbf{r}_s and 500 observation points \mathbf{r}_t are randomly distributed in two cubes satisfying the high frequency admissibility condition described in Sec. II-A. For each pair $(\mathbf{r}_s, \mathbf{r}_t)$, we evaluate the scalar Green’s function $G(\mathbf{r}_s, \mathbf{r}_t) = e^{-jk_0|\mathbf{r}_s - \mathbf{r}_t|} / |\mathbf{r}_s - \mathbf{r}_t|$, analytically and approximated with eq. (13). We define the approximation error of WNESA as $|\mathbf{G} - \mathbf{G}_{\text{WNESA}}|_2 / |\mathbf{G}|_2$, where \mathbf{G} and $\mathbf{G}_{\text{WNESA}}$ are two column vectors collecting the scalar Green’s function between all pairs of source/observation points, evaluated unapproximated and with WNESA, respectively; $|\mathbf{x}|_2$ indicates the ℓ^2 norm of vector \mathbf{x} . Fig. 4 shows plots of the approximation error when group size varies from one to 8λ : it is found that, once the number Q of equivalent

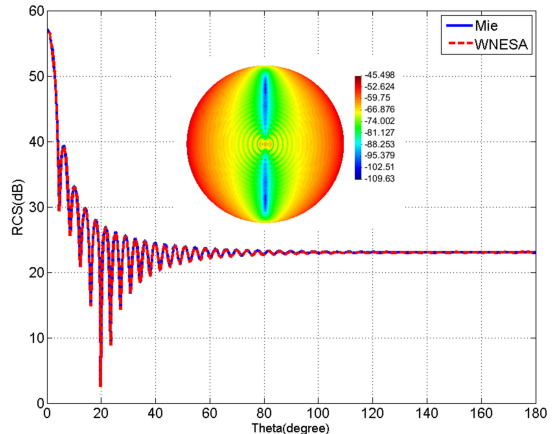


Fig. 6. Validation: RCS of a 16λ sphere, inset is the surface current, the direction of the direction of incident plane wave is $(\theta = 0^\circ, \phi = 0^\circ)$.

sources is fixed, accuracy increases with group size, differently from existing rank based methods [1]–[7], [13], [14].

Next, we test the ℓ^2 norm when approximating the EFIE impedance matrix. Without loss of generality, we chose two groups containing 636 and 527 RWG basis functions, respectively, and with size 1λ , extracted from the Octree clustering of a cylinder with diameter 1λ and height 8λ , discretized with 13168 unknowns. As a reference result we use a standard (unapproximated) MoM with a very accurate quadrature rule, with 61 Gaussian points on triangles. Fig. 5 shows the approximation error as a function of the number of equivalent sources Q : a number of equivalent sources $Q = 50$ yields the accuracy labeled as “Standard MoM, rule = (3,7)” in figure, which represents a “goal” accuracy, i.e. the accuracy achievable by a standard MoM with quadrature rule with 7 Gaussian points on the internal integral and 3 Gaussian points on the external integral (a typical accuracy of MoM codes). In all the following numerical experiments the number of equivalent sources is fixed as $Q = 50$.

Finally, we validate the accuracy by simulating the RCS of a sphere with diameter 16λ , under a plane wave illumination from the direction $(\theta = 0^\circ, \phi = 0^\circ)$; the surface of the sphere is discretized with 275463 unknowns. Here we use the combined field integral equation (CFIE), a four-level WNESA (two levels of low frequency algorithm and two levels of the directional algorithm) is employed to compress the CFIE impedance matrix directly; excellent agreement is found with respect to Mie series as shown in Fig. 6.

B. Computational Complexity

In order to numerically assess the computational cost of WNESA analyzed in Sec. II-E, we test a series of spheres with diameters equal to $8, 16, 32,$ and 64λ . We fix the discretization as $h/\lambda = 0.15$, which yields a number of unknowns equal to 17808, 71232, 284928, and 1139712, respectively. Four-, four-, five-, and five-level WNESA is employed, with two levels of low frequency algorithm in all cases. It should be noted here that the corresponding number of Octree levels is

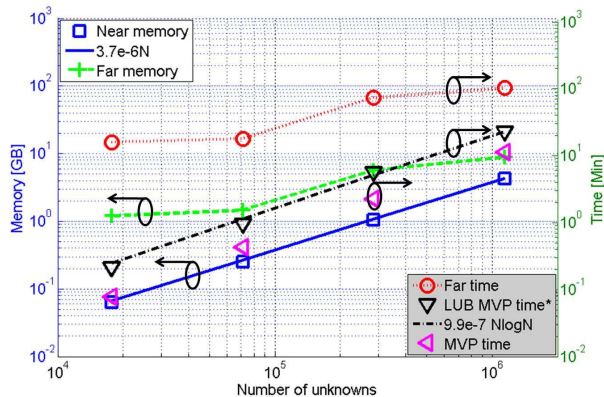


Fig. 7. Complexity scaling of WNESA for a series of spheres with diameters equal to 8, 16, 32, and 64 λ ; mesh discretization is fixed as $h/\lambda = 0.15$, corresponding to a number of unknowns equal to 17808, 71232, 284928, and 1139712.

(*): Least Upper Bound (LUB) for MVP, obtained by employing all possible directions at each level (not only directions in which at least a non-empty group is present); actual MVP time is always smaller than LUB.

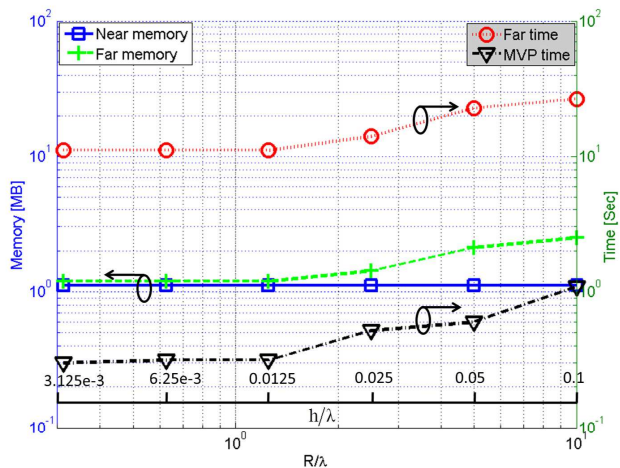


Fig. 8. Wideband performance: complexity as a function of electrical size with constant number of unknowns. Time and memory requirement for a series of spheres with electrical size $2R/\lambda$ 0.625, 1.25, 2.5, 5, 10, and 20, R is the radius; the number of unknowns is kept constant to $N=366672$, and h/λ varies accordingly as indicated. The graph shows that transition from low to high frequency regimes starts at $(R/\lambda = 1.25)$; a detailed description of this behavior is reported in sec. III-B.

4, 5, 6, and 7: however, the admissibility condition of the high frequency algorithm yields a smaller number of levels of WNESA (top levels of the Octree have an empty far interaction list). As a worst case scenario, we force the code to consider all possible directions d (not only directions including non-empty groups): this yields an upper bound to the actual cost. Fig. 7 summarizes the scaling: it is found that MVP costs $\mathcal{O}(N \log N)$, while setup time and storage requirements have a smaller cost, as explained above. It can be noticed that memory and factorization time for the two spheres with diameter 8λ and 16λ is almost constant (the same happens for spheres with diameter 32λ and 64λ): this is due to the fact that symmetry considerations allow to build and store the required operators (transfer/translation) for a single group at each WNESA level

(see Sec. II-D). Consequently, if the number of WNESA levels is constant, this cost remains constant too, as proven in fig. 7; the small increase in cost is a linear term due to the cost of radiation/receiving patterns at leaf level. On the other hand, the cost of MVP grows as $\mathcal{O}(N \log N)$, due to the fact that each translator/transfer matrix is multiplied a number of times corresponding to the number of non-empty groups at the considered level. Finally we also show the actual MVP time, i.e. MVP time when only translators in non-empty directions are considered: although it seems to scale “worse” than $\mathcal{O}(N \log N)$, its upper bound is the MVP time when all possible directions are taken into account, which has proven $\mathcal{O}(N \log N)$ complexity. This proves that MVP time has a cost bounded by $\mathcal{O}(N \log N)$.

We next test the wideband performance of WNESA; the scaling curves as a function of electrical size, for constant number of unknowns, are shown in Fig. 8. We test CPU time and memory requirements for a series of spheres with electrical size equal to 0.625, 1.25, 2.5, 5, 10, and 20 λ , and number of unknowns fixed to $N=366672$, corresponding to h/λ equal to 3.125e-3, 6.25e-3, 0.0125, 0.025, 0.05, and 0.1, respectively. It is worth stressing here that, because the number of unknowns N is kept constant, the number of Octree levels is constant too. Similarly, we also keep the number of equivalent sources Q constant. The first region, up to $R/\lambda \leq 1.25$, has constant CPU time and memory requirements for increasing electrical size; this corresponds to the low frequency regime, where only one direction is necessary to achieve the required precision [28]. Beyond this low frequency regime, CPU time and memory requirements increase because of the increasing number of directions N_d^l required to achieve the required precision; this confirms that the number of directions depends only on electrical group size, and not on the number of unknowns N . This can be explained by considerations similar to classical MLFMA [37]: high frequency asymptotic scaling assumes constant sampling of the surface (normalized w.r.t. wavelength), with a constant in front of $\mathcal{O}(N \log N)$ depending on a) meshing size and b) minimum group size. Nevertheless, Fig. 8 exemplifies how the algorithm adaptively transitions from low frequency to high frequency problems, with negligible time and memory increase (about a factor 3 in the case considered here).

C. Multiscale Benchmarking

In this section, we simulate a series of *Koch* snowflakes¹, a planar prefractal geometry where the number of different scales can be controlled by the iteration *level* of the fractal generator. We first analyze a 4-level snowflake at the frequency of 3 GHz; the dimensions of the snowflake in x and y directions are 1.0m and 1.15m, respectively, corresponding to 10 and 11.5 λ . It has been meshed with 3633 unknowns, with h/λ ranging from 9.9e-2 to 5.3e-1, and illuminated by a plane wave impinging from normal direction ($\theta^i = 0^\circ, \phi^i = 0^\circ$). Fig. 9 shows the surface current simulated by a two-level WNESA and full MoM: the error in the ℓ^2 norm is 0.008.

¹http://en.wikipedia.org/wiki/Koch_snowflake

TABLE III

MEMORY AND TIME CONSUMPTION FOR THE SERIES OF SNOWFLAKES WITH FRACTAL LEVEL VARYING FROM 4 TO 8 (THE EDGE OF THE GENERATING TRIANGLE IS 1M); FREQUENCY VARIES FROM 1GHZ TO 16GHZ, WITH CORRESPONDING ELECTRICAL SIZES EQUAL TO 3.8, 7.7, 15.4, 30.8, AND 61.6 λ . HERE WE FIX THE MESH SIZE h AS 0.12 λ , WITH A CORRESPONDING NUMBER OF UNKNOWNNS EQUAL TO 3102, 14340, 62415, 274791, AND 1083372, RESPECTIVELY.

| Frequency (GHz) | Fractal level | number of unknowns | number of low/high frequency levels | Near/Far field Memory | Far field approximation time[mm: ss] | Iteration number | MVP time[ss] |
|-----------------|---------------|--------------------|-------------------------------------|-----------------------|--------------------------------------|------------------|--------------|
| 1 | 4 | 3102 | 2/0 | 23/33 [MB] | 00: 06 | 5 | 0.04 |
| 2 | 5 | 14340 | 2/2 | 56/198 [MB] | 00: 23 | 4 | 0.8 |
| 4 | 6 | 62415 | 2/2 | 0.4/0.5 [GB] | 02: 03 | 4 | 4 |
| 8 | 7 | 274791 | 2/3 | 2.7/1.7 [GB] | 7: 54 | 5 | 17 |
| 16 | 8 | 1083372 | 2/3 | 16.5/5.6 [GB] | 24: 02 | 5 | 66 |

TABLE IV

MEMORY AND TIME CONSUMPTION FOR THE SERIES OF SNOWFLAKES WITH $level = 8$, WITH 1083372 UNKNOWNNS, AT 1, 2, 4, 8, AND 16 GHz; THE CORRESPONDING ELECTRICAL SIZES ARE 3.8, 7.7, 15.4, 30.8, AND 61.6 λ , RESPECTIVELY.

| Frequency (GHz) | number of low/high frequency levels | Near/Far field Memory[GB] | Far field approximation time[mm: ss] | Iteration number | MVP time[ss] |
|-----------------|-------------------------------------|---------------------------|--------------------------------------|------------------|--------------|
| 1 | 7/0 | 30.5/5.0 | 17: 00 | 11 | 12 |
| 2 | 5/2 | 30.5/5.2 | 17: 27 | 11 | 12 |
| 4 | 4/2 | 16.5/5.4 | 22: 10 | 27 | 35 |
| 8 | 2/3 | 16.5/5.5 | 22: 48 | 6 | 38 |
| 16 | 2/3 | 16.5/5.6 | 24: 02 | 5 | 66 |

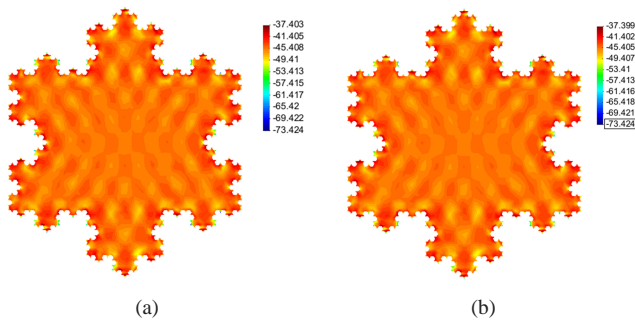


Fig. 9. Surface current (dBA/m) of the snowflake with $level = 4$; the number of unknowns is 3633, the direction of the incident plane wave is $(\theta = 0^\circ, \phi = 0^\circ)$, the ℓ^2 norm of the current simulated with WNESA with respect to full MoM is 0.008, (a) Full MoM (b) Two-level WNESA.

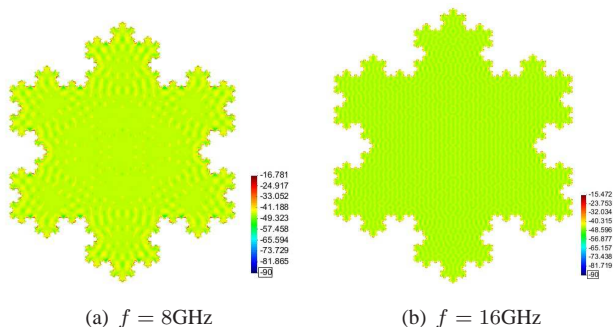


Fig. 10. Surface current (dBA/m) of the snowflake with $level = 7$ and $level = 8$, at the frequencies of 8 and 16 GHz (the number of unknowns is 274791 and 1083372, respectively, with corresponding electrical sizes of 30.8 λ and 61.6 λ). The direction of the incident plane wave is $(\theta = 0^\circ, \phi = 0^\circ)$.

We then run a series of tests by increasing the number of iterations of the pre-fractal generator together with the number of unknowns; we consider a series of snowflakes with fractal level ranging from 4 to 8 (the generating triangle has edge

equal to 1m), at the same time increasing the frequency from 1GHz to 16GHz. The corresponding electrical sizes are 3.8, 7.7, 15.4, 30.8, and 61.6 λ . Average mesh size is fixed as $h = 0.12\lambda$, yielding a number of unknowns equal to 3102, 14340, 62415, 274791, and 1083372, respectively. We stress the fact that the same algorithm is employed at all frequencies; the solver automatically selects the Octree levels corresponding to low and high frequency regimes (at low frequencies, WNESA simply degenerates to the algorithm described in [28]). The surface current density on the snowflakes at 8 and 16 GHz is shown in Fig. 10. To stabilize the ill-conditioning and accelerate convergence of the iterative solver, we precondition the system with MR-ILU [27], [38] preconditioner. Memory and time consumptions are summarized in Table III, which shows that our multiscale wideband algorithm keeps its effectiveness for high frequencies and increasing geometrical complexity.

We finally investigate the wideband performance of WNESA, by testing the 8-level snowflake at 1, 2, 4, 8, and 16 GHz, respectively, corresponding to growing electrical sizes 3.8, 7.7, 15.4, 30.8, and 61.6 λ . The system is preconditioned with MR-ILU [27], [38], and with the application of MR as detailed in [39] at the lowest frequencies (1-2 GHz), where low frequency (dense mesh) behavior is dominant. Simulation statistics are summarized in Table IV.

D. Validation by Modeling a Real Aircraft

In order to demonstrate the capability of WNESA to model high definition multiscale structures, a morphed P180 aircraft², shown in Fig. 11(a), has been analyzed. The aircraft is 12.1m long, and its wingspan is 13.8m, corresponding to, respectively, 27.6 and 31.5 λ at the analysis frequency of 686 MHz. All internal details, such as passenger seats, antenna array and the instruments board are considered in the

²<http://www.piaggioaero.com/#/en/products/p180-avanti-ii/overview>

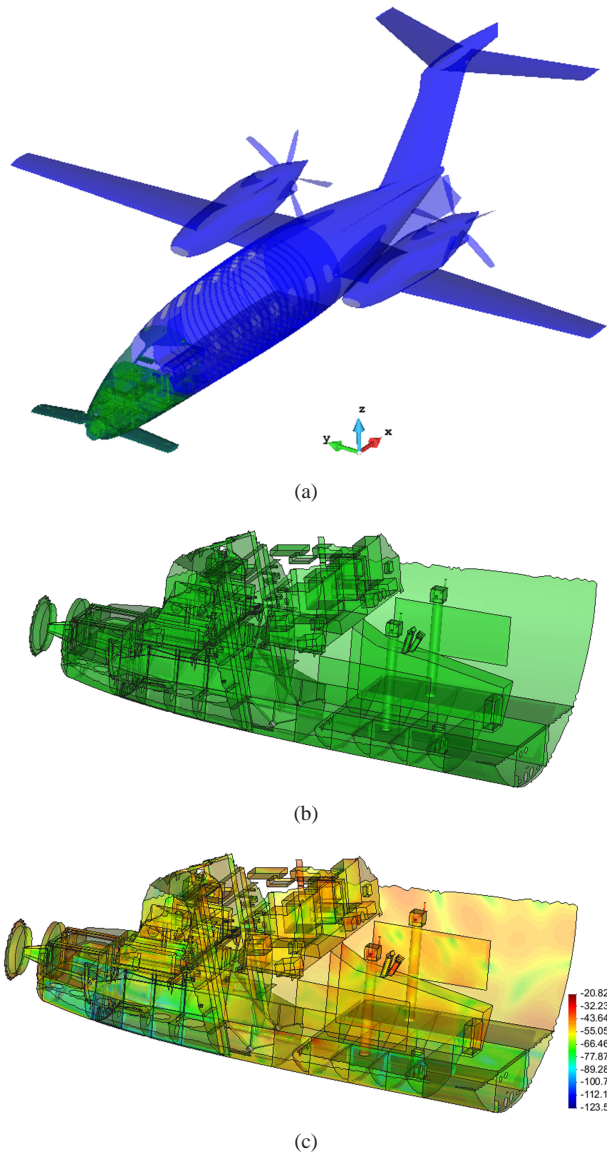


Fig. 11. Simulation of a 32λ long morphed P180 aircraft model, discretized with 1,086,083 unknowns, the incident direction of the plane wave is along the $+\hat{y}$ direction of the aircraft (a) mesh model, the green part is the instruments board in the nose, and the blue part is the body (b) details of the cockpit and nose, with instruments board (c) details of the surface current (dBA/m) of the cockpit and nose.

model. The aircraft is illuminated by a plane wave impinging along $+\hat{y}$ directions as in Fig. 11 (a), with the electric field polarized along \hat{z} . The model employs 1086083 unknowns, with discretization h/λ ranging from $2.3e-3$ to $8.0e-2$; a five-level WNESA (two levels at low frequency and three levels of the directional algorithm) is used to compress the EFIE impedance matrix, and the MR-ILU [27], [38] preconditioner, is employed. Factorization time and memory required are 1.8 hour and 9.1 GB; a flexible GMRES iterative solution is employed, with 10 inner iterations, with convergence to a residual of $1e-3$ reached in 100 iterations. The MVP time is 28 seconds, and overall solution time of the matrix equation amounts to 7.8 hours. Fig. 11 (b) and (c) shows the mesh model and surface current in [dBA/m] of the details of the

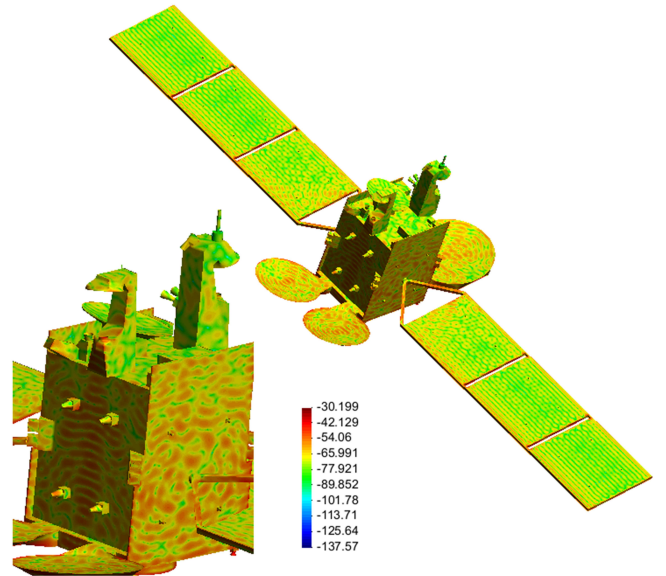


Fig. 12. Surface current (dBA/m) of the 80λ satellite model with 1,096,225 unknowns, the left-down corner is the details of its body. The incident direction of the plane wave is from the bottom of the satellite.

instruments board in the nose, respectively.

E. Validation by Modeling a Complex Satellite

Finally, we simulate a large and realistic model of the satellite object shown in Fig. 12. The largest dimension of the satellite is 20 meters, corresponding to 80λ at 1.2 GHz. Many details installed on the model have been considered in the model, yielding a high-fidelity model discretized with 1096225 unknowns, and h/λ ranges from $3.5e-3$ to $1.9e-1$. The satellite is illuminated by a plane wave impinging from the bottom, with the electric field polarized along $\hat{\theta}$. A six-level WNESA (two levels at low frequency and four levels of the directional algorithm) is used to compress the EFIE impedance matrix, and the MR-ILU [27], [38] preconditioner, is employed. Far field approximation time and memory are 32 mins and 10.6 GB; a flexible GMRES iterative solution is employed, with 10 inner iterations, with convergence to a residual of $1e-3$ reached in 76 iterations. The MVP time is 119 seconds, and overall solution time of the matrix equation for the satellite is 25.1 hours. Finally, Fig. 12 shows the current density on the surface of the satellite.

IV. CONCLUSION

In this work, we propose a wideband kernel-independent fast solver based on a nested equivalent source approximation (WNESA). The wideband nested approximation from child level to parent level is defined with an inverse-source process on the equivalent and testing surfaces. In order to obtain a fixed rank approximation method, we define different testing surfaces for coupling in low and high frequency regions. In the high frequency regime, the far coupling space is partitioned into directions spanning an angle $\mathcal{O}(\lambda/D_l)$. An $\mathcal{O}(N \log N)$ asymptotic complexity for both CPU time and memory requirements is derived and numerically proven. Besides, the

wideband solver presents excellent properties for the analysis of large and multiscale structures; numerical simulations of high-fidelity realistic problems prove the validity of the proposed WNESA.

APPENDIX

Algorithm 1 WNESA Low Rank Approximation

```

1: Initialize an Octree and directions
2: for  $l = L : 1 : -1$  do
3:   for  $e = 1 : N_d^l$  do
4:     if  $l = L$  then
5:        $\mathbf{V}^{L,d^e} \leftarrow$  radiation matrices with eq. (8)
6:        $\mathbf{U}^{L,d^e} \leftarrow$  receiving matrices with eq. (10)
7:     else
8:        $\mathbf{C}^{l,d^e} \leftarrow$  transfer matrices with eq. (14)
9:        $\mathbf{B}^{l,d^e} \leftarrow$  transfer matrices with eq. (15)
10:    end if
11:  end for
12:   $\mathbf{D}^l \leftarrow$  translation matrices with eq. (11) and (16)
13: end for

```

ACKNOWLEDGMENT

The authors would like to acknowledge Piaggio and IDS for providing the model of the morphed P180 aircraft, and the European Space Agency (ESA) for providing the satellite model (Emerald).

REFERENCES

- [1] S. Kapur and D. Long, "IES³: A fast integral equation solver for efficient 3-dimensional extraction," in *Proc. IEEE/ACM Int. Conf. Computer-Aided Design*, Nov. 1997, pp. 448–455.
- [2] M. Bebendorf and R. Venn, "A sparse matrix arithmetic based on H-matrices. part i: Introduction to H-matrices," *Computing*, vol. 62, no. 2, pp. 89–108, 1999.
- [3] M. Bebendorf, "Approximation of boundary element matrices," *Numer. Math.*, vol. 86, no. 4, pp. 565–589, 2000.
- [4] W. Hackbusch, B. N. Khoromskij, and S. A. Sauter, *On H²-matrices*. Springer, 2000.
- [5] K. Zhao, M. N. Vouvakis, and J.-F. Lee, "The adaptive cross approximation algorithm for accelerated method of moments computations of EMC problems," *IEEE Trans. Electromagn. Compat.*, vol. 47, no. 4, pp. 763–773, Nov. 2005.
- [6] J. M. Tamayo, A. Heldring, and J. M. Rius, "Multilevel adaptive cross approximation (MLACA)," *IEEE Trans. Antennas Propag.*, vol. 59, no. 11, pp. 4600–4608, Dec. 2011.
- [7] M. Li, C. Li, C.-J. Ong, and W. Tang, "A novel multilevel matrix compression method for analysis of electromagnetic scattering from PEC targets," *IEEE Trans. Antennas Propag.*, vol. 60, no. 3, pp. 1390–1399, Mar. 2012.
- [8] E. Bleszynski, M. Bleszynski, and T. Jaroszewicz, "AIM: Adaptive integral method for solving large-scale electromagnetic scattering and radiation problems," *Radio Sci.*, vol. 5, pp. 1225–1251, 1996.
- [9] S. Seo and J. Lee, "A fast IE-FFT algorithm for solving PEC scattering problems," *IEEE Trans. Magn.*, vol. 41, no. 5, pp. 1476–1479, May 2005.
- [10] J. R. Phillips and J. K. White, "A precorrected-FFT method for electrostatic analysis of complicated 3-D structures," *IEEE Trans. Computer-Aided Design of Integrated Circuits and Systems*, vol. 16, no. 10, pp. 1059–1072, 1997.
- [11] L. Greengard and V. Rokhlin, "A fast algorithm for particle simulations," *J. Comp. Phys.*, vol. 73, pp. 325–348, 1987.
- [12] J. Song, C. Lu, and W. Chew, "Multilevel fast multipole algorithm for electromagnetic scattering by large complex objects," *IEEE Trans. Antennas Propag.*, vol. 45, no. 10, pp. 1488–1493, Oct. 1997.

Algorithm 2 WNESA Matvec $\mathbf{y} = \mathbf{Z}\mathbf{I}$

```

1: Procedure WNESA Matvec ( $\mathbf{I}, \mathbf{y}$ )
2: for  $l = L : 1, -1$  do
3:   % Radiation Process
4:   if  $l = L$  then
5:     if  $l > l_{in}$  then
6:        $\zeta_{t^L}^L \leftarrow \zeta_{t^L}^L + \mathbf{V}_{t^L}^L \mathbf{I}_{t^L}$  % low frequency
7:     else
8:        $\zeta_{t^L}^{L,d^L} \leftarrow \zeta_{t^L}^{L,d^L} + \mathbf{V}_{t^L}^{L,d^L} \mathbf{I}_{t^L}$  % high frequency
9:     end if
10:   else
11:     if  $l > l_{in}$  then
12:        $\zeta_{t^l}^l \leftarrow \zeta_{t^l}^l + \mathbf{C}_{t^l}^l \zeta_{t^{l+1}}^{l+1}$  % low frequency
13:     end if
14:     if  $l = l_{in}$  then
15:        $\zeta_{t^l}^{l,d^l} \leftarrow \zeta_{t^l}^{l,d^l} + \mathbf{C}_{t^l}^{l,d^l} \zeta_{t^{l+1}}^{l+1}$  % interface
16:     end if
17:     if  $l < l_{in}$  then
18:        $\zeta_{t^l}^{l,d^l} \leftarrow \zeta_{t^l}^{l,d^l} + \mathbf{C}_{t^l}^{l,d^l} \zeta_{t^{l+1}}^{(l+1),ch(d^l)}$  % high frequency
19:     end if
20:   end if
21:   % Translation Process
22:   if  $l > l_{in}$  then
23:      $\xi_{s^l}^l \leftarrow \xi_{s^l}^l + \mathbf{D}_{s^l,t^l} \zeta_{t^l}^l$  % low frequency
24:   end if
25:   if  $l \leq l_{in}$  then
26:      $\xi_{s^l}^{l,d^l} \leftarrow \xi_{s^l}^{l,d^l} + \mathbf{D}_{s^l,t^l} \zeta_{t^l}^{l,-d^l}$  % high frequency
27:   end if
28: end for
29: % Receiving Process
30: for  $l = 1 : L$  do
31:   if  $l \neq L$  then
32:     if  $l > l_{in}$  then
33:        $\xi_{s^{l+1}}^{l+1} \leftarrow \xi_{s^{l+1}}^{l+1} + \mathbf{B}_{s^l}^l \xi_{s^l}^l$  % low frequency
34:     end if
35:     if  $l = l_{in}$  then
36:        $\xi_{s^{l+1}}^{l+1} \leftarrow \xi_{s^{l+1}}^{l+1} + \mathbf{B}_{s^l}^{l,d^l} \xi_{s^l}^{l,d^l}$  % interface
37:     end if
38:     if  $l < l_{in}$  then
39:        $\xi_{s^{l+1}}^{(l+1),ch(d^l)} \leftarrow \xi_{s^{l+1}}^{l+1} + \mathbf{B}_{s^l}^{l,d^l} \xi_{s^l}^{l,d^l}$  % high frequency
40:     end if
41:   else
42:     if  $l > l_{in}$  then
43:        $\mathbf{y}_{s^L}^L \leftarrow \mathbf{y}_{s^L}^L + \mathbf{U}_{s^L}^L \xi_{s^L}^L$  % low frequency
44:     else
45:        $\mathbf{y}_{s^L}^L \leftarrow \mathbf{y}_{s^L}^L + \mathbf{U}_{s^L}^{L,d^L} \xi_{s^L}^{L,d^L}$  % high frequency
46:     end if
47:   end if
48: end for
49:  $\mathbf{y} \leftarrow \mathbf{y}^L + \mathbf{Z}_{near} \mathbf{I}$  % Sum near interactions

```

- [13] E. Michielssen and A. Boag, "A multilevel matrix decomposition algorithm for analyzing scattering from large structures," *IEEE Trans. Antennas Propag.*, vol. 44, no. 8, pp. 1086–1093, Aug. 1996.
- [14] J. M. Rius, J. Parrn, A. Heldring, J. M. Tamayo, and E. Ubeda, "Fast iterative solution of integral equations with method of moments and matrix decomposition algorithm-singular value decomposition," *IEEE Trans. Antennas Propag.*, vol. 56, no. 8, pp. 2314–2324, Aug. 2008.
- [15] L. J. Jiang and W. C. Chew, "A mixed-form fast multipole algorithm," *IEEE Trans. Antennas Propag.*, vol. 53, no. 12, pp. 4145–4156, Dec. 2005.
- [16] H. Cheng, W. Y. Crutchfield, Z. Gimbutas, L. F. Greengard, J. F. Ethridge, J. Huang, V. Rokhlin, N. Yarvin, and J. Zhao, "A wideband fast multipole method for the helmholtz equation in three dimensions," *J. Comp. Phys.*, vol. 216, pp. 300–325, 2006.
- [17] I. Bogaert, J. Peeters, and F. Olyslager, "A nondirective plane wave MLFMA stable at low frequencies," *IEEE Trans. Antennas Propag.*, vol. 56, no. 12, pp. 3752–3767, Dec. 2008.
- [18] M. Vikram, H. Huang, B. Shanker, and T. Van, "A novel wideband FMM for fast integral equation solution of multiscale problems in electromagnetics," *IEEE Trans. Antennas Propag.*, vol. 57, no. 7, pp. 2094–2104, Jul. 2009.
- [19] V. Melapudi, B. Shanker, S. Seal, and S. Aluru, "A scalable parallel wideband MLFMA for efficient electromagnetic simulations on large scale clusters," *IEEE Trans. Antennas Propag.*, vol. 59, no. 7, pp. 2565–2577, Jul. 2011.
- [20] A. D. Baczewski, D. L. Dault, and B. Shanker, "Accelerated cartesian expansions for the rapid solution of periodic multiscale problems," *IEEE Trans. Antennas Propag.*, vol. 60, no. 9, pp. 4281–4290, Sep. 2012.
- [21] D. T. Schobert and T. F. Eibert, "Fast integral equation solution by multilevel green's function interpolation combined with multilevel fast multipole method," *IEEE Trans. Antennas Propag.*, vol. 60, no. 9, pp. 4458–4463, Sep. 2012.
- [22] M. Li, M. A. Francavilla, F. Vipiana, G. Vecchi, Z. Fan, and R. S. Chen, "A doubly hierarchical MoM for high-fidelity modeling of multiscale structures," *IEEE Trans. Electromagn. Compat.*, vol. 56, no. 5, pp. 1103–1111, Oct. 2014.
- [23] M. Messner, M. Schanz, and E. Darve, "Fast directional multilevel summation for oscillatory kernels based on Chebyshev interpolation," *J. Comp. Phys.*, vol. 231, pp. 1175–1196, 2012.
- [24] L. Ying, G. Biros, and D. Zorin, "A kernel-independent adaptive fast multipole algorithm in two and three dimensions," *J. Comp. Phys.*, vol. 196, pp. 591–626, 2004.
- [25] B. Engquist and L. Ying, "Fast directional multilevel algorithms for oscillatory kernels," *SIAM J. Sci. Comput.*, vol. 29, no. 4, pp. 1710–1737, 2007.
- [26] H. Chen, K. W. Leung, and E. K. N. Yung, "Fast directional multilevel algorithm for analyzing wave scattering," *IEEE Trans. Antennas Propag.*, vol. 59, no. 7, pp. 2546–2556, Jul. 2011.
- [27] M. A. Francavilla, F. Vipiana, G. Vecchi, and D. R. Wilton, "Hierarchical fast MoM solver for the modeling of large multiscale wire-surface structures," *IEEE Antennas Wireless Propag. Lett.*, vol. 11, pp. 1378–1381, 2012.
- [28] M. Li, M. A. Francavilla, F. Vipiana, G. Vecchi, and R. S. Chen, "Nested equivalent source approximation for the modeling of multiscale structures," *IEEE Trans. Antennas Propag.*, vol. 62, no. 7, pp. 3664–3678, Jul. 2014.
- [29] M. Bebendorf and R. Venn, "Constructing nested bases approximations from the entries of non-local operators," *Numer. Mathem.*, vol. 121, no. 4, pp. 609–635, 2012.
- [30] M. Bebendorf, C. Kuske, and R. Venn, "Wideband nested cross approximation for Helmholtz problems," *Technical Report SFB 611 Preprint*, 2012.
- [31] J. Araque and G. Vecchi, "Field and source equivalence in source reconstruction on 3D surfaces," *Prog. Electromagn. Res.*, vol. 103, pp. 67–100, 2010.
- [32] W. C. Chew and C. C. Lu, "The use of Huygens' equivalence principle for solving the volume integral equation of scattering," *IEEE Trans. Antennas Propag.*, vol. 41, no. 7, pp. 897–904, Jul. 1993.
- [33] B. Engquist and L. Ying, "Fast directional algorithms for the helmholtz kernel," *J. Comput. Appl. Math.*, vol. 234, no. 6, pp. 1851–1859, 2010.
- [34] S. M. Rao, D. R. Wilton, and A. W. Glisson, "Electromagnetic scattering by surfaces of arbitrary shape," *IEEE Trans. Antennas Propag.*, vol. 30, no. 3, pp. 409–418, May 1982.
- [35] L. Dagum and R. Menon, "OpenMP: an industry standard API for shared-memory programming," *Computational Science & Engineering, IEEE*, vol. 5, no. 1, pp. 46–55, 1998.
- [36] The MPI Forum, "MPI: A message-passing interface standard," Knoxville, TN, USA, Tech. Rep., 1994.
- [37] E. Darve, "The fast multipole method I: Error analysis and asymptotic complexity," *SIAM J. Num. Anal.*, vol. 38, no. 1, pp. 98–128, 2000.
- [38] F. Vipiana, M. A. Francavilla, and G. Vecchi, "EFIE modeling of high definition multiscale structures," *IEEE Trans. Antennas Propag.*, vol. 58, no. 7, pp. 2362–2374, Jul. 2010.
- [39] M. A. Echeverri Bautista, F. Vipiana, and G. Vecchi, "A hierarchical fast solver for EFIE-MoM analysis of multiscale structures at very low frequencies," *IEEE Trans. Antennas Propag.*, vol. 62, no. 2, pp. 1523–1528, 2014.



Mengmeng Li received the B.S. degree (with honors) in physics from Huaiyin Normal College, Huaiian, China, in 2007, and Ph.D. degree in electromagnetic field and microwave technology from Nanjing University of Science and Technology, Nanjing, China in 2014.

From 2012 to 2014 he carried out fast solver for multiscale simulations as a visiting student at Electronics Department, Politecnico di Torino and Antenna and EMC Lab (LACE), Istituto Superiore Mario Boella (ISMB), Torino, Italy. His research interests focus on fast solver algorithms, computational electromagnetic solvers for circuits, signal integrity analysis, and multiscale simulations. Since 2014, he has been with the the Department of Communication Engineering, Nanjing University of Science and Technology, as Assistant Professor.

Mr. Li received the Student Paper Award (top 5 of 260) at the International Conference on Microwave and Millimeter Wave Technology in 2012.



Matteo Alessandro Francavilla (M'14) received the Laurea degree in Telecommunication Engineering and Ph.D. degree in applied electromagnetics from Politecnico di Torino, Italy, respectively in 2007 and 2011. During 2007 he spent six months with the Netherlands Organization for Applied Scientific Research (TNO), The Hague, The Netherlands.

During 2010 he carried out part of the Doctoral research as a visiting student at the University of Houston, TX, USA. Since January 2011, he has been working as a researcher at the Antenna and EMC Lab (LACE), at the Istituto Superiore Mario Boella (ISMB), Torino, Italy. His scientific interests include integral equations, numerical techniques for antennas, fast solvers, preconditioners, periodic structures and layered media analysis.

PLACE
PHOTO
HERE

Rushan Chen (M'01) was born in Jiangsu, China. He received the B.Sc. and M.Sc. degrees from the Department of Radio Engineering, Southeast University, China, in 1987 and 1990, respectively, and the PhD degree from the Department of Electronic Engineering, City University of Hong Kong, in 2001.

He joined the Department of Electrical Engineering, Nanjing University of Science and Technology (NJUST), China, where he became a Teaching Assistant in 1990 and a Lecturer in 1992. Since September 1996, he has been a Visiting Scholar with the Department of Electronic Engineering, City University of Hong Kong, first as Research Associate, then as a Senior Research Associate in July 1997, a Research Fellow in April 1998, and a Senior Research Fellow in 1999. From June to September 1999, he was also a Visiting Scholar at Montreal University, Canada. In September 1999, he was promoted to Full Professor and Associate Director of the Microwave and Communication Research Center in NJUST, and in 2007, he was appointed Head of the Department of Communication Engineering, NJUST. He was appointed as the Dean in the School of Communication and Information Engineering, Nanjing Post and Communications University in 2009. And in 2011 he was appointed as Vice Dean of the School of Electrical Engineering and Optical Technique, Nanjing University of Science and Technology. His research interests mainly include microwave/millimeter-wave systems, measurements, antenna, RF-integrated circuits, and computational electromagnetics. He has authored or coauthored more than 200 papers, including over 140 papers in international journals.

Dr. Chen received the 1992 third-class science and technology advance prize given by the National Military Industry Department of China, the 1993 third-class science and technology advance prize given by the National Education Committee of China, the 1996 second-class science and technology advance prize given by the National Education Committee of China, and the 1999 first-class science and technology advance prize given by Jiangsu Province, as well as the 2001 second-class science and technology advance prize. He is the recipient of the Foundation for China Distinguished Young Investigators presented by the National Science Foundation (NSF) of China in 2003. In 2008, he became a Chang-Jiang Professor under the Cheung Kong Scholar Program awarded by the Ministry of Education, China. Besides, he was selected as a member of Electronic Science and Technology Group by academic degree commission of the State Council in 2009. Dr. Chen is a Senior Member of the Chinese Institute of Electronics (CIE), Vice-Presidents of Microwave Society of CIE and IEEE MTT/APS/EMC Nanjing Chapter. He serves as the reviewer for many technical journals such as IEEE Trans. on AP and MTT, Chinese Physics etc., and now serves as an Associate Editor for the International Journal of Electronics.

PLACE
PHOTO
HERE

Giuseppe Vecchi (M'90- SM'07- F'10) received the Laurea and Ph.D. (Dottorato di Ricerca) degrees in electronic engineering from the Politecnico di Torino, Torino, Italy, in 1985 and 1989, respectively, with doctoral research carried out partly at Polytechnic University (Farmingdale, NY). He was a Visiting Scientist with Polytechnic University in 1989-1990, and since 1990 he is with the Department of Electronics, Politecnico di Torino, where he has been Assistant Professor, Associate Professor (1992-2000), and Professor. He was a Visiting Scientist at

the University of Helsinki, Helsinki, Finland, in 1992, and has been an Adjunct Faculty in the Department of Electrical and Computer Engineering, University of Illinois at Chicago, since 1997. His current research activities concern analytical and numerical techniques for analysis, design and diagnostics of antennas and devices, RF plasma heating, electromagnetic compatibility, and imaging.